

Journal Pre-proof

Benzenesulfonyl incorporated chalcones: Synthesis, structural and optical properties

Jean M.F. Custodio, Fernando Gotardo, Wesley F. Vaz, Giulio D.C. D'Oliveira, Leonardo Rodrigues de Almeida, Ruben D. Fonseca, Leandro H.Z. Cocca, Caridad N. Perez, Allen G. Oliver, Leonardo de Boni, Hamilton B. Napolitano



PII: S0022-2860(20)30169-1

DOI: <https://doi.org/10.1016/j.molstruc.2020.127845>

Reference: MOLSTR 127845

To appear in: *Journal of Molecular Structure*

Received Date: 12 December 2019

Revised Date: 30 January 2020

Accepted Date: 3 February 2020

Please cite this article as: J.M.F. Custodio, F. Gotardo, W.F. Vaz, G.D.C. D'Oliveira, L.R. de Almeida, R.D. Fonseca, L.H.Z. Cocca, C.N. Perez, A.G. Oliver, L. de Boni, H.B. Napolitano, Benzenesulfonyl incorporated chalcones: Synthesis, structural and optical properties, *Journal of Molecular Structure* (2020), doi: <https://doi.org/10.1016/j.molstruc.2020.127845>.

This is a PDF file of an article that has undergone enhancements after acceptance, such as the addition of a cover page and metadata, and formatting for readability, but it is not yet the definitive version of record. This version will undergo additional copyediting, typesetting and review before it is published in its final form, but we are providing this version to give early visibility of the article. Please note that, during the production process, errors may be discovered which could affect the content, and all legal disclaimers that apply to the journal pertain.

© 2020 Published by Elsevier B.V.

CRediT author statement

Jean M. F. Custodio: Conceptualization, Methodology, Supervision, Writing - Review & Editing

Fernando Gotardo: Formal analysis, Investigation, Writing - Original Draft.

Wesley F. Vaz: Writing - Original Draft

Giulio D. C. D'Oliveira: Writing - Original Draft.

Leonardo Rodrigues de Almeida: Writing - Original Draft

Ruben D. Fonseca: Writing - Original Draft

Leandro H. Z. Cocca: Writing - Original Draft

Caridad N. Perez: Supervision, Writing - Review & Editing, Resources

Allen G. Oliver: Supervision, Writing - Review & Editing, Resources

Leonardo de Boni: Writing - Review & Editing, Resources

Hamilton B. Napolitano: Supervision, Writing - Review & Editing

Benzenesulfonyl Incorporated chalcones: Synthesis, Structural and Optical Properties

Authors

Jean M. F. Custodio^{a*}, Fernando Gotardo^b, Wesley F. Vaz^c, Giulio D. C. D'Oliveira^a, Leonardo Rodrigues de Almeida^b, Ruben D. Fonseca^{bd}, Leandro H. Z. Cocca^b, Caridad N. Perez^a, Allen G. Oliver^e, Leonardo de Boni^b and Hamilton B. Napolitano^{c*}

^aInstituto de Química, Universidade Federal de Goiás, Goiania, Goiás, Brazil

^bInstituto de Física de São Carlos, Universidade de São Paulo, Sao Paulo, Sao Paulo, Brazil

^cCiências Exatas e Tecnológicas, Universidade Estadual de Goiás, Anapolis, Goiás, Brazil

^dCampus Universitario, Universidad Popular del Cesar, Barrio Sabana, Valledupar, Colombia

^eChemistry and Biochemistry, University of Notre Dame, Notre Dame, Indiana, 46556, USA

Correspondence email: jeanmfcustodio@gmail.com; hbnapolitano@gmail.com

Synopsis A set of new sulfonamide chalcones hybrids is presented. Their structural and optical properties are investigated

Abstract Although the optical properties and applicability of chalcones as potential nonlinear optics (NLO) materials is well known, hybrids having both chalcone and sulfonamide portions are relatively scarce yet. In this sense, we are seeking to show if combining both into a double functionalized compound will still have similar or better NLO responses. For this, we have synthesized three sulfonamide-chalcone analogues by changing the substituent bonded to the sulfonamide ring (I = ethoxy; II = Cl and III = Br). These compounds were characterized by spectroscopic methods (NMR, IR and HRMS) and thermal methods (HSM and DSC/TGA). Their crystal structures were determined by Single Crystal X-ray Diffraction (SCXRD) and their molecular structures were compared. Crystallographic results showed that one compound crystallizes in a triclinic system whereas the others crystallize in a monoclinic crystal system. Moreover, their crystal packing is dominated by C–H···O interactions. In addition to this study and to first characterize these compounds, linear and nonlinear optical (NLO) properties were performed in all three compounds dissolved in dimethyl sulfoxide. One-photon and two-photon absorption (2PA) spectra and incoherent second harmonic generation were obtained by employing different spectroscopic techniques. The interesting results observed in the linear and NLO measurements showed that different groups bounded to the same main backbone did not significantly modify their

optical properties, although they strongly affect their crystal structures. σ 2PA spectra reveal that the first excited state is allowed by both 1PA and 2PA, which indicates asymmetry in the charge distribution along the π -conjugated molecule structure. NLO properties of compounds I-III agree with other chalcones previously studied, which indicates that adding the benzenosulfonyl group does not influence these properties. Considering the similar experimental values for different substituents, these results motivate further investigation on substituent-based optical properties for other sulfonamide-chalcone hybrids.

Keywords: Sulfonamide chalcone; nonlinear optical properties; hybrid compounds

1. Introduction

Chalcones and their derivatives have been extensively studied because of their wide range of applicability. The presence of the reactive keto-ethylenic group and two aryl rings linked by an enone group is responsible for most of the biological properties observed for these compounds (Tajuddeen *et al.*, 2018; Singh *et al.*, 2014). Many biological potentials, such as anticancer (Kamal *et al.*, 2012; Custodio *et al.*, 2018), antituberculosis (Lin *et al.*, 2002), antileishmanial (Zhai *et al.*, 1999) and therapeutical (Mahapatra & Bharti, 2016) have been attributed to chalcones, and their use as potential optical devices has also been studied. Chalcones have delocalized electronic charge distribution and π -orbitals; this leads to a high electron density mobility making them ideal candidates for nonlinear optical (NLO) materials (Shetty *et al.*, 2018).

Not only is the chalcones backbone, but also the substitution pattern around their aromatic rings is responsible for observed NLO properties. Abegão and co-workers reported an increase in the 2-photon absorption (2PA) and hyper-Rayleigh scattering (HRS) of two chalcones when an aromatic hydrogen atom was replaced by the radical methoxyl (Abegão *et al.*, 2016). Also, chalcones derivatives with different groups (Br and NO₂) presented different third order susceptibility χ^3 and second order hyperpolarizability γ_h when measured using picosecond laser pulses by Z-scan technique (D'silva *et al.*, 2012). Similar, structural changes in chalcone derivatives can modify different optical properties such as refractive index, absorption magnitude and spectral position, as well the optical energy gap (Makhlouf *et al.*, 2018). These examples indicate that even with same backbone, structurally modified chalcones can exhibit variable physical properties. Furthermore, some examples of optically active sulfonamide compounds are known. Polymeric materials containing sulfonamide-substituted azobenzene chromophores were investigated and found to have good NLO response (Ražna *et al.*, 1999); benzene sulfonamide derivatives have also shown good NLO activity (Sarojini *et al.*, 2013). Beyond experimental

results, theoretical calculations determined for this class of compounds have also provided excellent simulations (Govindasamy & Gunasekaran, 2015).

Although the optical properties and applicability of chalcones as potential NLO materials is well known, double functionalized compounds having both chalcone and sulfonamide portions are relatively scarce. Having in mind these results for chalcones and sulfonamides separately, we are seeking to show if combining both into a double functionalized compound will still have similar or better NLO responses. Herein, we present a new set of benzenesulfonyl incorporated chalcones with the same π -conjugated backbone bearing distinct charge groups. The synthesized molecules are sulfonamide chalcones, which are (*E*)-*N*-(2-(3-(4-ethoxyphenyl)-1-(2-(phenylsulfonylamine)phenyl)prop-2-en-1-one) (I), (*E*)-3-(4-chlorophenyl)-1-(2-(phenylsulfonylamine) phenyl)prop-2-en-1-one (II) and (*E*)-3-(4-bromophenyl)-1-(2-(phenylsulfonylamine)phenyl)prop-2-en-1-one (III). In addition to their structural study, these compounds were fully characterized using a variety of spectroscopic techniques, such as ^{13}C and ^1H Nuclear Magnetic Resonance (NMR), Infrared (IR), High Resolution Mass Spectroscopy (HRMS), Differential Scanning Calorimetry (DSC), Thermogravimetric Analysis (TGA) and Hot Stage microscopy (HSM). We determined the linear and nonlinear optical properties of all compounds dissolved in dimethyl sulfoxide. One-photon (1PA) and two-photon absorptions (2PA), as well as incoherent molecular second harmonic generation, were measured to elucidate the dependence of these properties with the molecular structure.

2. Experimental

2.1. Materials and Apparatus

^1H NMR and ^{13}C NMR spectra were recorded by a 400 MHz Bruker Avance III 11.75 T NMR spectrometer. Infrared studies were performed with a PerkinElmer Frontier Dual Range FTIR/IR Spectrometer, measured in Attenuated Total Reflectance mode. Mass spectrometric analyses were performed using a MicroTOF-Q® III spectrometer equipped with a commercial ESI ion source (Bruker Daltonics, Bremen, Germany). The degree of purity of the compounds was determined from the ^1H NMR spectrum, by peak area integration assigned to the structure and the total area of all peaks attributed to the material under analysis.

Fluorescence and linear absorption over the UV-Vis-NIR region were performed in solution, respectively, by using HITACHI F7000 fluorimeter and SHIMADZU UV-1800 spectrometer. The solutions were prepared with the samples dissolved in dimethyl sulfoxide (DMSO) in a concentration of about 10^{-5} mol/L. For both measurements, a fused silica cuvette with optical path length of 10 mm was used as solution confinement tool.

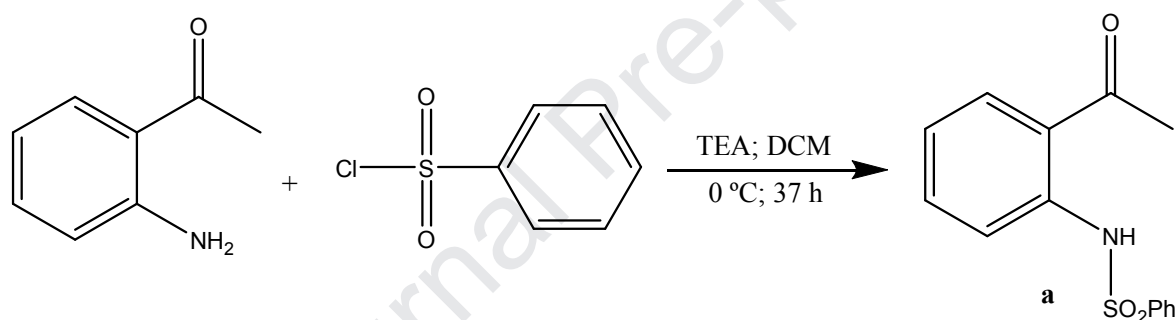
2.2. Synthesis and Crystallization

2.2.1. General procedures

2'-N-phenylsulfonylacetophenone (**a**), was synthesized by reaction between benzenesulfonyl chloride and 2-aminoacetophenone in dichloromethane (Scheme 1), based on a literature preparation previously described (de Castro *et al.*, 2017). Compounds **I-III** were synthesized using the methodology reported by Castro (De Castro *et al.*, 2016) via base catalysis (Scheme 2).

2.2.2. Synthesis of the intermediate 1-(2-(phenylsulfonylamino)phenyl) ethanone (**a**)

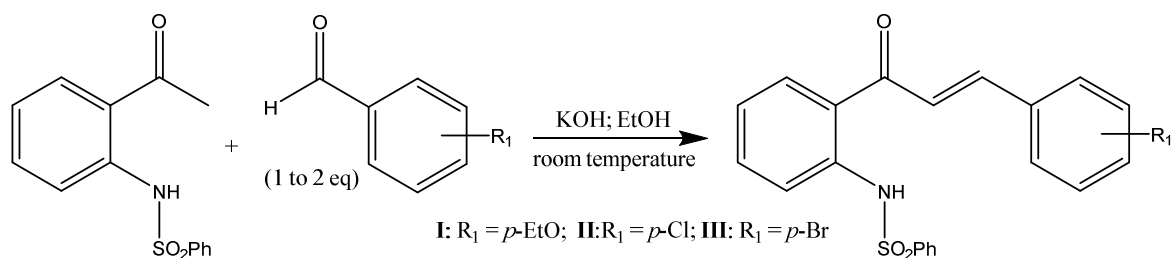
Benzenesulfonyl chloride (70.65 g, 0.40 mol), 2-aminoacetophenone (67.58 g, 0.50 mol) and triethylamine (50.55 g, 0.50 mol) were dissolved in 500 mL of dichloromethane and kept in the refrigerator for 37 h, following Scheme 1. The solution was filtered and the resulting crystals rinsed with methanol.



Scheme 1 General conditions for the synthesis of 2'-N-phenylsulfonylacetophenone (**a**)

2.2.3. Synthesis of compounds **I, II and III**

Precursor **a**, the substituted benzaldehyde and catalytic amount of potassium hydroxide (141 mmol.L^{-1}) reacted at room temperature. Then, water (0.08 L) and hydrochloric acid were added, following Scheme 2. The product was extracted with dichloromethane and the crystals were obtained by direct evaporation of this solution. The benzaldehyde, time of reaction and amount of each reactant are presented in Table S1.



Scheme 2 General conditions for the synthesis of compounds **I**, **II** and **III**.**2.3. Physico-chemical Characterization**

1-(2-(phenylsulfonylamino)phenyl) ethanone (a): Yield, 55.1 g (50.1%) of a white crystalline solid. ¹H NMR (CDCl₃) δ 2.56 (s, 3H), δ 7.08 (ddd, *J* 7.98 Hz, 7.33 Hz, 1.18 Hz, 1H), 7.42 – 7.46 (m, 2H), 7.46 (dddd, *J* 8.44 Hz, 7.34 Hz, 1.56 Hz, 0.41 Hz, 1H), 7.51 – 7.54 (m, 1H), 7.70 (ddd, *J* 8.40 Hz, 1.15 Hz, 0.45 Hz, 1H), 7.80 (ddd, *J* 8.01 Hz, 1.59 Hz, 0.46 Hz, 1H), 7.84 – 7.87 (m, 2H), 11.50 (s, 1H); ¹³C NMR (CDCl₃) δ 28.17, 119.25, 122.41, 122.77, 127.24, 129.05, 131.91, 133.01, 134.97, 139.48, 139.92, 202.43; HRMS (High-Resolution Mass Spectrometry) calculated for [C₁₄H₁₂NO₃S + H]⁺ 276.0694, found 276.0725.

(E)-N-(2-(3-(4-ethoxyphenyl)-1-(2-(phenylsulfonylamino)phenyl)prop-2-en-1-one (I): Yellow crystalline solid, yield 76.1%, purity of 98.1%, mp 137 – 140 °C. ¹H NMR (CDCl₃) δ 1.45 (t, *J* 7.00 Hz, 3H), δ 4.09 (q, *J* 7.00 Hz, 2H), δ 6.91 – 6.94 (m, 2H), δ 7.13 (ddd, *J* 1.25 Hz, 7.38 Hz, 7.88 Hz, 1H), δ 7.20 (d, *J* 15.50 Hz, 1H), δ 7.35 – 7.39 (m, 2H), δ 7.40 – 7.44 (m, 1H), δ 7.47 (ddd, *J* 1.45 Hz, 7.40 Hz, 8.38 Hz, 1H), δ 7.53 – 7.56 (m, 2H), δ 7.65 (d, *J* 15.50 Hz, 1H), δ 7.75 (dd, *J* 1.03 Hz, 8.33 Hz, 1H), δ 7.80 – 7.84 (m, 3H), δ 11.22 (s, 1H) (Fig S1 and Table S2); ¹³C NMR (CDCl₃) δ 14.7, 63.8, 115.0, 119.5, 120.9, 123.2, 125.3, 127.0, 127.3, 129.0, 130.4, 130.5, 132.8, 134.0, 139.5, 139.7, 146.1, 161.6, 192.7 (Fig S2 and Table S3); IR 1637 (m), 1497 (m), 1329 (s), 927 (m), 761 (s); HRMS calculated for [C₂₃H₂₁NO₄S + Na]⁺ 430.1089, found 430.1103.

(E)-3-(4-chlorophenyl)-1-(2-(phenylsulfonylamino)phenyl)prop-2-en-1-one (II): Yellow crystalline solid, yield 70.9%, purity of 98.2%, mp 150 – 155 °C. ¹H NMR (CDCl₃) δ 7.14 (ddd, *J* 1.16 Hz, 7.34 Hz, 7.94 Hz, 1H), δ 7.33 (d, *J* 15.55 Hz, 1H), δ 7.37 – 7.42 (m, 4H), δ 7.43 – 7.46 (m, 1H), δ 7.50 (ddd, *J* 1.55 Hz, 7.40 Hz, 8.40 Hz, 1H), δ 7.52 – 7.55 (m, 2H), δ 7.63 (d, *J* 15.55 Hz, 1H), δ 7.75 (dd, *J* 1.08 Hz, 8.33 Hz, 1H), δ 7.82 – 7.85 (m, 3H), δ 11.18 (s, 1H) (Fig S3 and Table S2); ¹³C NMR (CDCl₃) δ 120.7, 122.5, 123.2, 124.6, 127.3, 129.0, 129.4, 129.7, 130.6, 132.9, 132.9, 134.5, 137.0, 139.5, 140.0, 144.5, 192.5 (Fig S4 and Table S3); IR 1641 (m), 1492 (m), 1329 (m), 928 (m), 756 (m); HRMS calculated for [C₂₁H₁₆ClNO₃S + H]⁺ 398.0618, found 398.0462.

(E)-3-(4-bromophenyl)-1-(2-(phenylsulfonylamino)phenyl)prop-2-en-1-one (III): Yellow crystalline solid, yield 52.0%, purity of 97.1%, mp 157 – 159 °C. ¹H NMR (CDCl₃) δ 7.14 (ddd, *J* 1.15 Hz, 7.35 Hz, 7.90 Hz, 1H), δ 7.34 (d, *J* 15.55 Hz, 1H), δ 7.37 – 7.40 (m, 2H), δ 7.42 – 7.47 (m, 3H), δ 7.49 (ddd, *J* 1.54 Hz, 7.34 Hz, 8.41 Hz, 1H), δ 7.55 – 7.58 (m, 2H), δ 7.61 (d, *J* 15.55 Hz, 1H), δ 7.75 (dd, *J* 0.80 Hz, 8.35

H_z , 1H), δ 7.81 – 7.84 (m, 3H), δ 11.17 (s, 1H) (Fig S5 and Table S2); ^{13}C NMR ($CDCl_3$) δ 120.7, 122.6, 123.2, 124.6, 125.4, 127.3, 129.0, 129.9, 130.6, 132.4, 132.9, 133.3, 134.5, 139.4, 140.0, 144.5, 192.5 (Fig S6 and Table S3); IR 1640 (m), 1489 (m), 1331 (m), 924 (m), 751 (s); HRMS calculated for $[C_{21}H_{16}BrNO_3S + H]^+$ 442.0113, found 442.0004.

2.4. Refinement

Single crystals of **I** were selected and mounted in an Agilent SuperNova diffractometer, whereas for single crystals of **II** and **III** a Bruker APEX II CCD diffractometer was used. Data were recorded with graphite-monochromated MoK α radiation ($\lambda = 0.71073 \text{ \AA}$) at room temperature. The data collection, cell refinements and data reduction were performed using *CrysAlis PRO* (Rigaku, 2015) for **I**, and SAINT software (Bruker, 2009) for **II** and **III**. The structures were solved with ShelXS (Sheldrick, 2008) by direct methods and refined with ShelXL (Sheldrick, 2015) by least squares minimization. As implemented in Olex2 (Dolomanov *et al.*, 2009) all the hydrogen atoms were placed in calculated positions and refined with fixed individual displacement parameters [$U_{iso}(H) = 1.2U_{eq}(C)$ or $1.5U_{eq}(C)$] according to the riding model. The structural analysis was performed using Mercury (Macrae *et al.*, 2008). The possible interactions and hydrogen bonds were checked by using PARST (Nardelli, 1995) and PLATON (Spek, 2009). The crystallographic information files of **I**, **II** and **III** were deposited in the Cambridge Structural Data Base (CCDC) (Allen, 2002; Groom & Allen, 2014) under the codes 1949073, 1949070, 1949072, respectively. Copies of the data can be obtained, free of charge, via www.ccdc.cam.ac.uk.

2.5. Nonlinear optical measurements

2.5.1. Two-Photon Absorption

Z-Scan technique (Sheik-Bahae *et al.*, 1990), using a tunable 120 femtosecond coherent light source, was employed to determine two-photon absorption (2PA) cross section spectra. This technique consists of measuring the transmittance as function of the position of the sample along the z-direction, focusing the laser beam by a convergent lens. The transmittance is normalized by taking the ratio of the transmittance at z-positions over the transmittance far from the focus, thus the normalized transmittance ($T(z)$) is calculated by:

$$T(z) = \frac{1}{\sqrt{\pi}q_0(z, 0)} \int_{-\infty}^{\infty} \ln[1 + q_0(z, 0)e^{-t^2}] dt \quad (1)$$

in which, z is the position of the sample with respect to the focus ($z = 0$), $q_0 = \alpha_{2PA} I_0 L \left(1 + \frac{z^2}{z_0^2}\right)^{-1}$. I_0 is the intensity of the laser pulse, z_0 is the Rayleigh length, L is the optical path length, and α_{2PA} is the nonlinear absorption coefficient. The 2PA cross section (σ_{2PA}) can be calculated by:

$$\sigma_{2PA} = \frac{\hbar\omega}{N} \alpha_{2PA} \quad (2)$$

in which, ω is the frequency of the light, \hbar is Planck constant, and N is the density of molecules per cm^3 . The unit used for the 2PA cross section is GM (Göppert-Mayer; $1 \text{ GM} = 1 \times 10^{-50} \text{ cm}^4 \cdot \text{s} \cdot \text{photon}^{-1}$) (Göppert-Mayer, 2009).

To perform this experiment, the experimental setup includes a tunable optical amplifier (TOPAS), a Ti:Sapphire (CPA 2001 from Clark-MXR Inc.) laser, silicon photodetectors and locking amplifiers. The Ti:Sapphire emits at 775 nm wavelength with a pulsewidth of 150 fs in a repetition rate of 1 kHz. It is used to pump TOPAS, which tunes the wavelength of the light in a range from 470 nm to 800 nm with pulsewidths of about 120 fs. A 15 cm convergent lens focuses this tuned light in the region that the sample is translated. Two Silicon photodetectors are used to collect signals from the Z-Scan measurements; one uses to measure the transmitted light for each position, z , of the sample, and other used as reference of laser intensity fluctuations. Locking amplifiers amplify and average the signals from the two photodetectors in order to increase the signal:noise ratio.

2.5.2. Incoherent second harmonic generation (First order hyperpolarizability)

The first hyperpolarizability (β) of the chalcone derivatives was determined by the Hyper-Rayleigh Scattering technique (HRS) (Clays & Persoons, 1992; Franzen *et al.*, 2008) in which a Nd:YAG Q-Switched and mode-locked laser that delivers a train of pulses at 1064 nm wavelength was employed. This pulse train contains of about 30 pulses of 100 ps each, separated by 13.2 ns from each other (Franzen *et al.*, 2008). Laser was set to operate at 100 Hz of repetition rate. Pulses are focalized at the sample that scatters the second harmonic (532 nm) of the incident light and then is collected by a photomultiplier positioned at an angle of 90° with the incident light. In addition to that, an optical filter centered at 532 nm with 10 nm of bandwidth is positioned in front of the photomultiplier to block extra light that could interfere with the desired signal. The intensity of the scattered light, $I(2\omega)$, and the incident laser light, $I(\omega)$, are related by:

$$I(2\omega) = \sum_{i=1}^M G N_i \beta_i^2 I^2(\omega) \quad (3)$$

in which, G is an instrumental constant determined during experimental setup based on a well-known standard sample, and N_i is the molecular concentration. The calibration sample chosen was *para*-Nitroaniline (pNA) dissolved in DMSO that presents a $\beta(1064nm) = 26.2 \times 10^{-30} \text{ cm}^5/\text{esu}$ (Franzen *et al.*, 2008). Acquisition of data for several concentration of a chalcone derivative gives a linear relation between $I(2\omega)$ and N_i , in which an angular coefficient ($\alpha_{chalcone}$) is determined. The angular coefficient of the pNa (α_{pNA}) can be found by repeating this procedure for different pNa molecular concentrations. The first hyperpolarizability of the chalcone ($\beta_{chalcone}$) is related to these angular coefficients by:

$$\beta_{chalcone} = \sqrt{\beta_{pNa}^2 \frac{\alpha_{chalcone}}{\alpha_{pNA}}} \quad (4)$$

in which, $\alpha_{chalcone} = G\beta_{chalcone}^2$ and $\alpha_{pNA} = G\beta_{pNA}^2$.

2.6. Thermal characterization

Thermogravimetric analyses (TGA) were carried out on a Shimadzu TGA-60 thermobalance, using approximately 5.0 mg of sample placed on aluminium pans and heated from room temperature up to 500 °C, at 10 °C.min⁻¹, under nitrogen flow (50 mL.min⁻¹). Differential scanning calorimetric (DSC) measurements were performed on a Shimadzu DSC-60 instrument. Samples (2.5 ± 0.5 mg) were placed at aluminium pans and heated from room temperature up to 400 °C, at 10 °C min⁻¹, under nitrogen flow (50 mL.min⁻¹). All data were processed using the Shimadzu TA-60 thermal data analysis software (version 2.2). Hot-stage microscopy (HSM) was performed on a Leica DM2500P microscope connected to an Linkam T95-PE hot-stage apparatus. Data were visualized with the Linksys 32 software for hot stage control. The crystals of compounds **I**, **II** and **III** were placed on a 13 mm glass coverslip, placed on a 22 mm diameter pure silver heating block inside of the stage. The samples were heated at a ramp rate of 10 °C.min⁻¹ up to a temperature required to melting of all material.

3. Results and discussion

3.1. Solid state characterization

The synthesized compounds have a common chalcone backbone, composed of two aromatic rings connected through a three-carbon bridge (with one α,β -unsaturation) having a keto carbonyl group, and an *o*-benzenesulfonamide group attached to ring A. Compounds **I-III** differ each other by the substituent at *p*-position of ring C (**I** = OEt, **II** = Cl, and **III** = Br). Compound **I** crystallizes in the space group $P2_1/c$

whereas **II** and **III**, each with two independent molecules (α and ω) in asymmetric unit, crystallize in space group $P\bar{1}$. Experimental details are shown in Table 1 and their ORTEP diagrams are presented in Fig. 1.

Table 1 Crystal structure and refinement data of **I**, **II** and **III**

	(I)	(II)	(III)
Table 2			
Crystal data			
Chemical formula	$C_{23}H_{21}NO_4S$	$C_{21}H_{16}ClNO_3S$	$2(C_{21}H_{16}BrNO_3S)$
M_r	407.47	397.86	884.63
Crystal system, space group	Monoclinic, $P2_1/c$	Triclinic, $P1$	Triclinic, $P1$
Temperature (K)	294	296	296
a, b, c (Å)	8.8384 (5), 26.6514 (16), 8.7741 (4)	8.4130 (4), 9.8066 (5), 13.1211 (7)	8.5051 (9), 12.1557 (15), 19.520 (2)
α, β, γ (°)	90, 90.963 (5), 90	73.231 (2), 85.049 (2), 69.892 (2)	101.955 (4), 99.056 (4), 92.558 (4)
V (Å ³)	2066.5 (2)	973.22 (9)	1943.5 (4)
Z	4	2	2
Radiation type	Mo $K\alpha$	Mo $K\alpha$	Mo $K\alpha$
μ (mm ⁻¹)	0.19	0.32	2.24
Crystal size (mm)	× ×	0.48 × 0.40 × 0.28	0.42 × 0.30 × 0.29
Data collection			
Diffractometer	SuperNova, Dual, Cu at zero, AtlasS2	Bruker APEX-II CCD	Bruker APEX-II CCD
Absorption correction	Multi-scan <i>CrysAlis PRO</i> 1.171.38.46	Multi-scan <i>SADABS2014/5</i> (Bruker,2014/5)	Multi-scan <i>SADABS2014/5</i> (Bruker,2014) was

	(Rigaku Oxford Diffraction, 2015) Empirical absorption correction using spherical harmonics, implemented in SCALE3 ABSPACK scaling algorithm.	was used for absorption correction. wR2(int) was 0.1499 before and 0.0735 after correction. The Ratio of minimum to maximum transmission is 0.8342. The $\lambda/2$ correction factor is 0.00150.	used for absorption correction. wR2(int) was 0.1590 before and 0.0451 after correction. The Ratio of minimum to maximum transmission is 0.7271. The $\lambda/2$ correction factor is 0.00150.
T_{\min}, T_{\max}	0.686, 1.000	0.622, 0.745	0.542, 0.745
No. of measured, independent and observed [$I >$ $2\sigma(I)$] reflections	71464, 5570, 4391	37156, 4007, 2917	68586, 7942, 5855
R_{int}	0.039	0.050	0.038
$(\sin \theta/\lambda)_{\text{max}}$ (\AA^{-1})	0.694	0.626	0.625
Refinement			
$R[F^2 > 2\sigma(F^2)],$ $wR(F^2), S$	0.054, 0.131, 1.11	0.044, 0.121, 1.02	0.040, 0.102, 1.03
No. of reflections	5570	4007	7942
No. of parameters	267	248	495
No. of restraints	0	0	36
H-atom treatment	H atoms treated by a mixture of independent and constrained refinement	H atoms treated by a mixture of independent and constrained refinement	H atoms treated by a mixture of independent and constrained refinement
$\Delta\rho_{\text{max}}, \Delta\rho_{\text{min}}$ (e \AA^{-3})	0.28, -0.29	0.30, -0.26	0.73, -0.75

Computer programs: *CrysAlis PRO* 1.171.38.46 (Rigaku OD, 2015), *SHELXS* (Sheldrick, 2008), *SHELXL* (Sheldrick, 2015), *Olex2* (Dolomanov *et al.*, 2009).

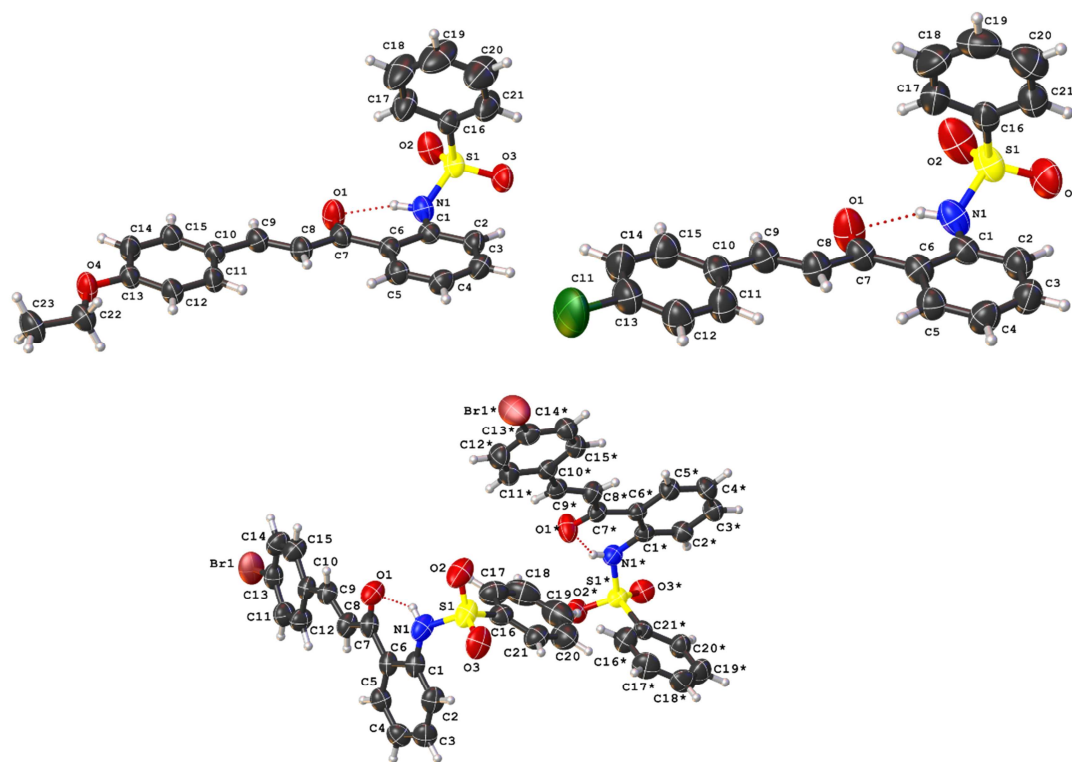


Figure 1 The ORTEP diagram of ellipsoids at 50% probability level with the atomic numbering scheme for the asymmetric unit of **I** (a), **II** (b) and **III** (c). The atomic numbering labels for ω molecule (c) is equal to α molecule but differ by asterisk (*) symbol. Hydrogen atoms are represented as spheres with arbitrary radii and its labels attributed followed the corresponding attached atom

Molecular planarity is an important parameter and should be considered when studying the physical properties of a compound. Nevertheless, higher the number of donor-receptor interactions in a molecule, better will be the electron transfer and nonlinearity. Thus, more planar is a molecule with conjugated π -electrons bridge, more these characteristic interactions will be expected to occur (Kumar *et al.*, 2011; Menezes *et al.*, 2015). **I** and **II** could be considered planar molecules, observing that the angle between the planes of rings A and B in these molecules are 4.56° and 7.72° respectively. Meanwhile in **III**, the α molecule also could be considered planar, with angle equal to 4.24° . However, in ω , this planarity is decreased, and the rings form an angle of 16.37° . An overlay of molecules **I**, **II**, **III- α** and **III- ω** is depicted in Fig. 2. There are four previously reported structures of *o*-sulfonamide-chalcones (de Castro *et*

al., 2017). One of them (ref-code: QERNEJ, here mentioned as NAB) has only substituents at *para* position of the ring B. Structural parameters of NAB and **I**, **II**, and **III** differ each other by the angle formed between rings A and B, as well as the torsion angle N1-S1-C16-C17.

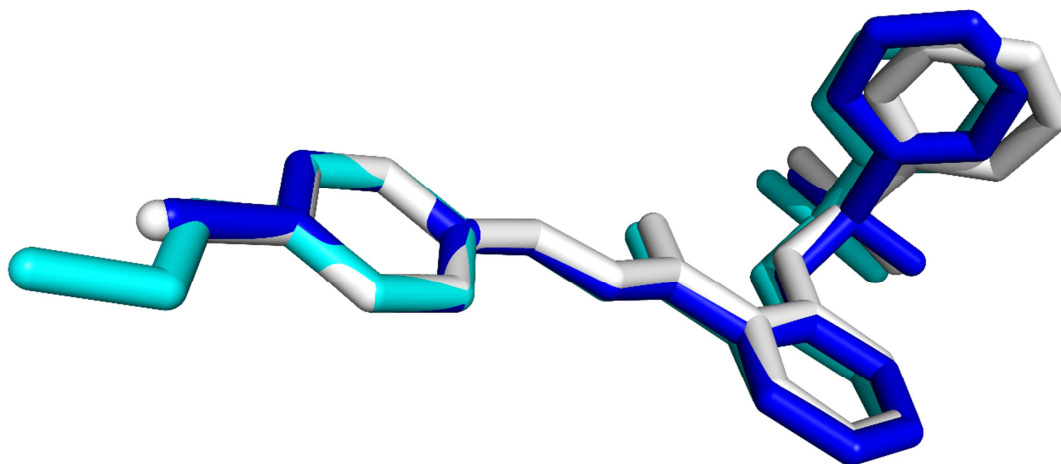


Figure 2 Conformational differences between the compounds **I** [cyan], **II** [blue], **III α** [white] and **III σ** [black]

The crystal packings of **I**, **II** and **III**, shown in Fig. 3, are dominated by C–H \cdots O interactions, as shown in Table 2, leading to a dimer-stabilized arrangement and bifurcated intermolecular interactions. Such arrangements are also present in similar compounds (de Castro *et al.*, 2017; Castro *et al.*, 2013; Seo *et al.*, 2010; Custodio, Vaz *et al.*, 2019; De Castro *et al.*, 2016; Custodio *et al.*, 2018). The crystal packing of **I** (Fig. 4a) is stabilized by three C–H \cdots O interactions involving the atom O2 and chains along the *c*-axis. Similar to NAB, the aromatic ring C is almost perpendicular (74.03°) to the plane formed by the chalcone backbone along this chain. In contrast, the C–H \cdots O interactions in the extended structure of **II** (Fig. 4b) is composed of dimers with $R_2^2(14)$ motif, involving SO₂ group and the ring A, through C8–H8 \cdots O2 and C12–H12 \cdots O1 interactions (Fig. 4c). Thus, the crystal packing in **II** is stabilized by a chain parallel to the *a*-axis. In addition, the dimer has an inversion center which orients the C rings in opposite directions.

Table 3 Non-classical hydrogen-bond geometry (Å, °) for **I**, **II** and **III**.

<i>D</i> –H \cdots <i>A</i>	<i>D</i> –H	H \cdots <i>A</i>	<i>D</i> \cdots <i>A</i>	<i>D</i> –H \cdots <i>A</i>
I				
C8–H8 \cdots O2 ⁱ	0.93	2.47	3.355 (2)	159
C5–H5 \cdots O2 ⁱ	0.93	2.56	3.399 (2)	150
C11–H11 \cdots O2 ⁱ	0.93	2.54	3.388 (2)	151
II				

C8—H8...O2 ⁱⁱ	0.93	2.49	3.308 (3)	148
C12—H12...O1 ⁱⁱ	0.93	2.53	3.360 (3)	148
C3—H3...O3 ⁱⁱⁱ	0.93	2.65	3.418 (3)	141
III				
C8—H8...O2 ⁱⁱ	0.93	2.41	3.283 (3)	156
C11—H11...O2 ⁱⁱ	0.93	2.49	3.262 (4)	140
C12—H12...O1 ⁱⁱ	0.93	2.59	3.442 (4)	153
C8*—H8*...O2* ⁱⁱ	0.93	2.49	3.321 (3)	148
C14*—H14*...O1* ⁱⁱ	0.93	2.61	3.422 (4)	147

Symmetry code: (i) $x, y, z+1$; (ii) $x+1, y, z$; (iii) $-x+1, -y+1, -z+2$.

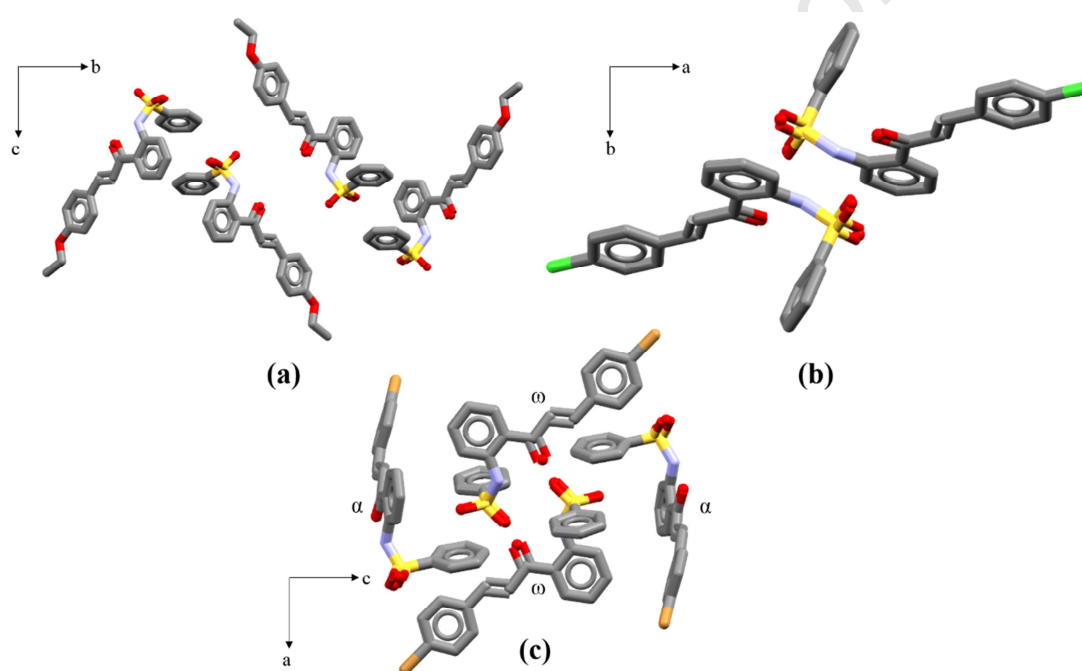


Figure 3 Molecular packing of **I** (a), **II** (b) and **III** (c).

On the other hand, in the packing of **III**, there are, in α molecule, two C—H...O contacts leading to propagation parallel to the a -axis (Fig 4d). The first involves SO₂ group and H atoms of ring B (C11—H11...O2) and vinyl group (C8—H8...O2) forming a $R_2^1(7)$ motif, whereas C12—H12...O1 interaction involves carbonyl group and H atom of ring B. About ω molecule, C8*—H8*...O2* and C14*—H14*...O1* interactions form a $R_2^2(14)$ motif parallel to a -axis (Fig. 4e).

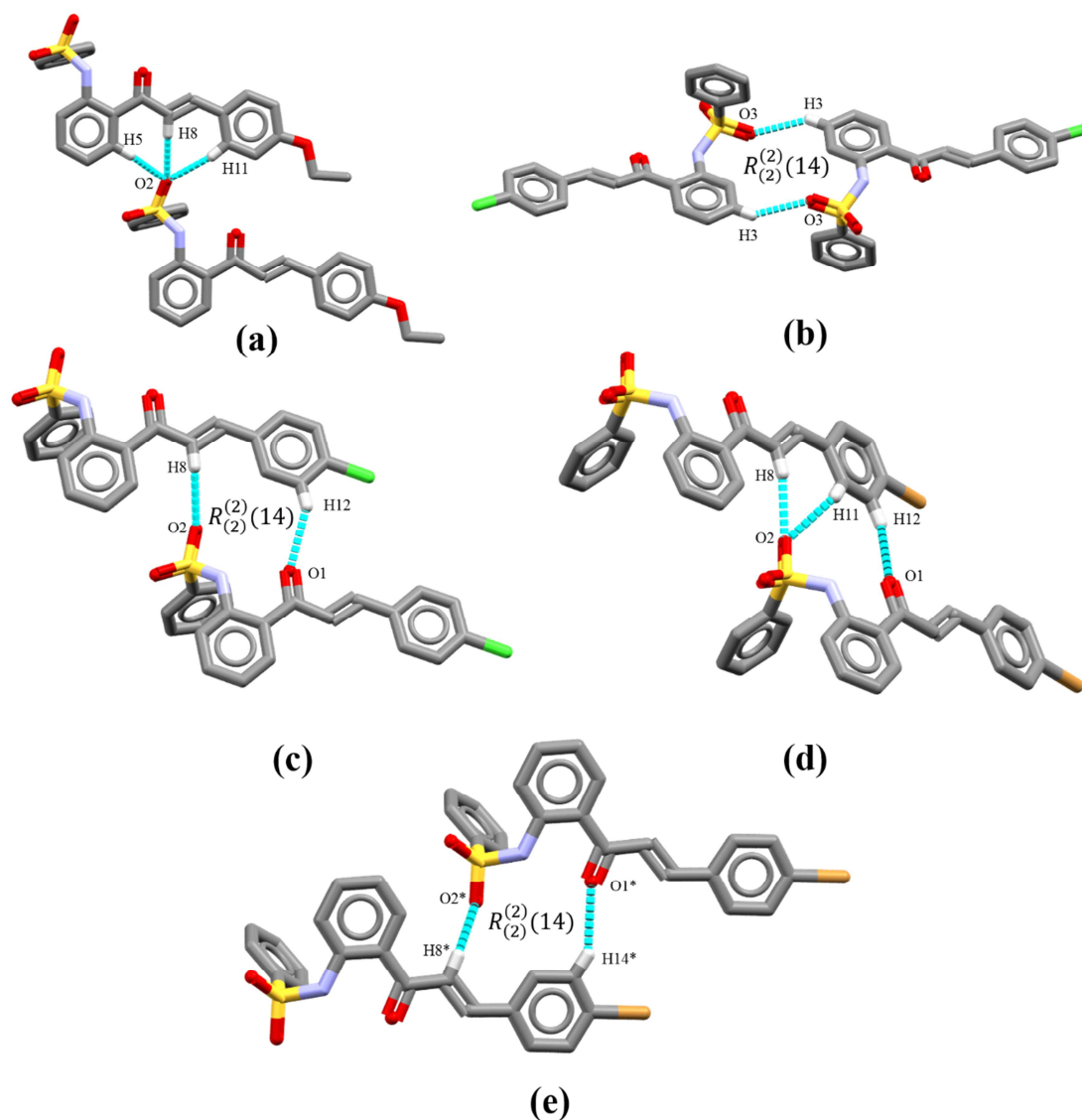


Figure 4 C-H...O interactions present in the crystal packing of **I**, **II** and **III**.

3.2. One-, two-photon absorption spectra and molecular second harmonic generation.

Fluorescence emission signals for all three sulfonamide chalcones dissolved in DMSO solvent were not observed by exciting the sample at different wavelengths in the absorption bands. This indicates that the decay from the first singlet excited state to the ground state take place in a nonradioactive relaxation process when molecules are in DMSO solutions. Figure 5 shows molar absorptivities (dashed blue lines) of the three chalcones derivatives, in which the lower electronic transition is located around 355 nm for molecule **I**, and it is blue shifted of about 30 nm for molecules **II** and **III**, now located at 320 nm.

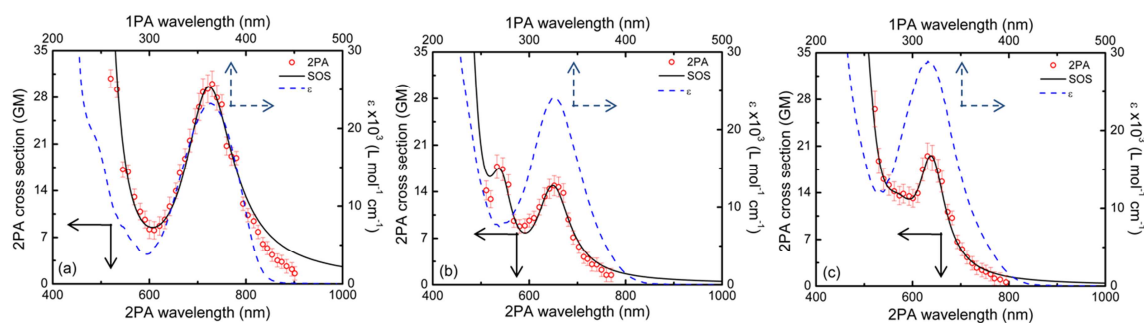


Figure 5 Molar absorptivity (ϵ) (dashed blue lines) and two-photon absorption cross section (open red circles) spectra of chalcones **I** (a), **II** (b) and **III** (c) dissolved in DMSO solvent. The black lines are the adjustments obtained with Sum-Over-States model. Molar absorptivity was measured using a concentration of 10^{-4} mol.L $^{-1}$ at room temperature.

Maximum values of the molar absorptivity were found to be of about 23000 mol $^{-1}$ L cm $^{-1}$ for molecule **I** (see Fig. 5(a)), and for molecules **II** and **III** (see Fig.5(b) and (c) respectively) of about 25000 and 28000 mol $^{-1}$ L cm $^{-1}$ respectively. For wavelengths longer than 500 nm, the compounds do not present any additional absorption bands at the UV-VIS-NIR region. Furthermore, Fig. 5 also depicts 2PA spectra (open red circles) along with their Sum Over States approach model adjustment (continuous black line). Each open red circle is the two-photon absorption cross section value obtained by adjusting the Z-Scan measurements with Eq. (1). As can be seen, the lowest energetic 2PA band matches with the lowest energetic one photon absorption, which indicates that the electronic state is allowed by one- and two-photon absorption spectrum. The charge asymmetry in the sulfonamide chalcones allows that the transition selection rules for the dipole electric moment, in this type of conjugated molecules, may be relaxed, permitting an electronic state to absorb one or two-photons.

The 1PA absorption is red-shifted for molecule **I** with respect to molecules **II** and **III**, this effect may be assigned by the higher molecular planarity combined with the electronegativity of the ethoxy group when compared to bromine and chlorine atoms. However, changes between chlorine and bromine atoms, in the *para* position of the sulfonamide chalcones, do not modify significantly both molar absorption magnitude and, as well, the energy value of the lowest energetic band. As mentioned before, a small red-shift is observed only for chalcone with ethoxy group, indicating a small reduction in the energy of the lowest electronic state. Similar characteristics are also observed in the 2PA spectrum: the highest 2PA cross section of about 26 GM at 720 nm (see Fig. 5(a)) was observed for **I** and it is red-shifted, as well, when compared to **II** and **III**, following the same behavior of 1PA absorption.

Compounds **II** and **III**, showed small values of about 14 GM and 17 GM respectively (Fig. 5(b) and (c)). These two molecules present a two-photon allowed-band centered approximately at 560 nm with maximum values of 18 GM and 14 GM respectively. This band does not have a similar in the 1PA at 280 nm, which means that the electronic state located at 280 nm is allowed by 2PA. This band was not measured for compound **I** due to the red-shift of the lowest energetic state. Also, all 2PA spectrum presented a monotonically increase of the 2PA cross sections for wavelengths shorter than 510 nm, which is caused by the resonance enhancement effect. This effect occurs when the photon energy is close in energy to the first excited transition state, increasing the 2PA probability to occur.

Both, one- and two-photon absorption results indicate that the electronic states of the chalcones were not affected by replacing chlorine atom with bromine. Only the ethoxy group showed a slight difference between the three molecules. This can be explained by the distinct electronegativities of the different substituents, which should be responsible by different charge distribution in the molecules. As can be seen in the structures of **I**, **II** and **III**, the main molecular skeleton is identical for all, which may indicates, *a priori*, the same conjugation length. However, the reduction in planarity can also decrease the magnitude of the one- and two-photon absorption cross sections as well blue shift the optical transitions. As mention in section 3.1 (Solid state characterization), molecule **III** shows to have the lower degree of planarity comparing to the other two molecules, when **III** is in ω conformation. However, the optical properties show to be close in values between all three samples, which indicates that in solution, molecule **III** majority conformation may be α . In summary, as the main structures look essentially the same, it is expected that optical properties should also be similar in magnitude.

The transition dipole moment related to the lowest electronic state, which gives the strength of the transition was evaluated considering the experimental molar absorptivity. As all sulfonamide chalcones studied here present one absorption band at approximately 350 nm (lowest energy band), the transition dipole moment related to the transition from the ground state to the first singlet excited state, μ_{01} , is determined by:

$$\mu_{01}^2 = \frac{3 \cdot 10^3 \ln(10) \hbar c n}{(2\pi)^3 N_A \omega_{01}} \frac{1}{L^2} \int \varepsilon(\omega) d\omega \quad (5)$$

in which, c is the speed of light, \hbar is Planck's constant, N_A is Avogadro's number, ω_{01} is the transition frequency of the first excited state, n is the refraction index of solvent (for DMSO, $n = 1,42$), $L^2 = \frac{3n^2}{2n^2+1}$ is the Onsager local field factor (Onsager, 1936), and ε is the molar absorptivity. Calculated values for μ_{01} are depicted in Table 3 together with other parameters determined by Sum-Over-States approach, this one used to describe the 2PA spectra and is explained later.

Table 4 Permanent dipole momentum difference and transition dipole momentum for three compounds studied in this work, in Debye unit.

Compounds	μ_{01}	$\Delta\mu_{01}$	μ_{12}	μ_{13}
I	6.2	9.0	7.8	-
II	7.3	5.1	2.3	3.7
III	8.4	4.2	3.2	5.0

Combining μ_{01} and the 2PA spectrum, it is possible to determine additional information about the molecules and charge distribution at different excited states by determining the magnitude of transition dipoles moments from the higher excited states, μ_{12} and μ_{13} respectively. Additionally, the difference of permanent dipole momentum between the first excited state and the ground state, $\Delta\mu_{01} = \mu_{11} - \mu_{00}$, can also be evaluated. These parameters were phenomenologically determined by employing Sum-Over-State (SOS) approach (Kamada *et al.*, 2003; Neves *et al.*, 2007) and, for this purpose, the two-photon absorption spectra were phenomenologically adjusted (solid black line at Fig. 5) by using:

$$\sigma_{2PA}^{SOS}(\omega) = \frac{128 \pi^5}{5(chn)^2} L^4 \frac{\omega^2}{(\omega_{01} - \omega)^2 + \Gamma_{01}^2} \left[\frac{|\mu_{01}|^2 \Delta\mu_{01}^2 \Gamma_{01}}{(\omega_{01} - 2\omega)^2 + \Gamma_{01}^2} + \frac{|\mu_{12}|^2 |\mu_{01}|^2 \Gamma_{02}}{(\omega_{02} - 2\omega)^2 + \Gamma_{02}^2} + \frac{|\mu_{13}|^2 |\mu_{01}|^2 \Gamma_{03}}{(\omega_{03} - 2\omega)^2 + \Gamma_{03}^2} \right] \quad (6)$$

in which, ω_{0n} represents the transition frequency from ground state to excited state n ; n can assume values 1, 2 and 3. Γ_{0n} is the damping constant corresponding to the same n transition, and ω is the laser frequency. In most cases, the damping constant for organic molecules in the UV-VIS is about 0.3 eV and it was used in this work to all states. Terms inside of the brackets describe the states involved in the 2PA spectra. The product of the transition dipole moments is related to the amplitude of the 2PA band, and μ_{01} is a fixed parameter obtained from the linear absorption. This makes the others transition dipoles to be determined independent of each other. The parameters obtained with the SOS model combined with the 2PA spectra (solid black line, Fig. 5) are listed at Table 3. It is important to say that the first electronic state energy was obtained from the linear absorption spectra, which gave values of 3.5 eV for **I**, 3.8 eV for **II** and 3.9 eV for **III**. The energy of the second 2PA band calculated to be of approximately 4.43 eV was obtained from the 2PA spectra, related to a electronic state located at 280 nm. For the third band, we used the energy of about 6 eV, related to an electronic state at approximately 205 nm.

Both, transition dipole moments and the difference of permanent dipole moment between first excited state and ground state, are similar in magnitude to other chalcones already reported (Lemes *et al.*, 2018; Abegão *et al.*, 2016), as well to small conjugated organic molecules, such as oxyzoles (Abegão *et al.*, 2018). The highest value of $\Delta\mu_{01}$, obtained for molecule **I**, explains the red shift observed in the 1PA and

2PA spectra, as well as the highest magnitude of molar absorptivity and 2PA cross section. It indicates that the charges distribution is more delocalized on the ground and first excited states compared with other two molecules. Also, the slightly higher planarity of **I** is in agreement with the increment of $\Delta\mu_{01}$.

First hyperpolarizability values of the chalcone derivatives at 1064 nm were obtained with Hyper-Rayleigh scattering measurements (HRS). Calibration of the experimental setup was performed by using the well-known *para*-nitroaniline (pNA) compound dissolved in the same solvent as the chalcones studied. HRS signals, illustrated as symbols in the inset of Fig. 6(a), have a quadratic dependence of the generated nonlinear scattered signal, $I(2\omega)$, at 532 nm as a function of the laser intensity, $I(\omega)$, at 1064 nm. The inset also depicts for sample **I** distinct quadratic results (different colors) which are related to different solute concentrations. Solid lines represent the best second order polynomial fittings. All other samples and pNA standard molecule have shown similar graphics.

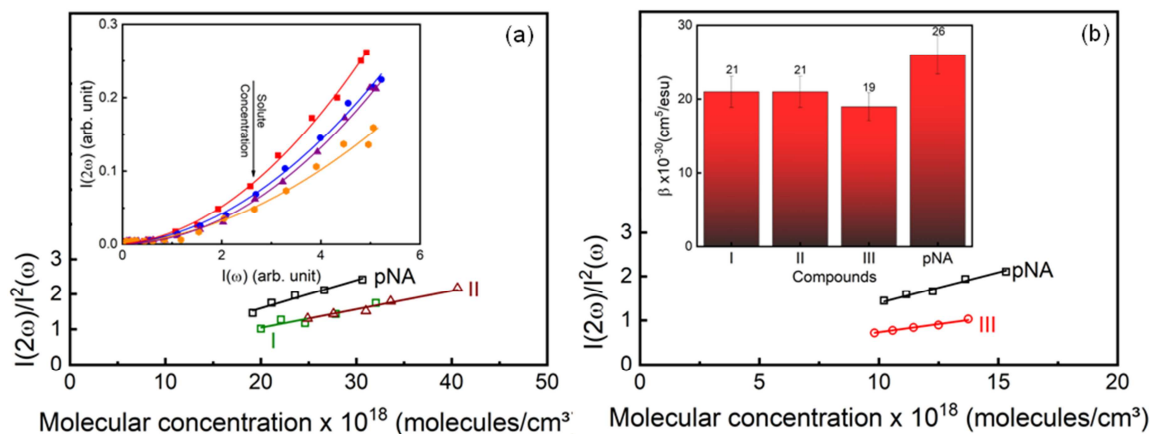


Figure 6 Linear dependence of $I(2\omega)/I^2(\omega)$ as function of the molecular concentrations for pNA (squares) and chalcone derivatives: **I** (green square), **II** (wine triangles) and **III** (red circles). Lines represent the best linear fits. The inset, in (a), represents the first hyperpolarizability scattering signals as a function of the pump intensity for distinct molar concentrations of sample **III**. Lines are the best second order polynomial fits. Similar curves were obtained for the other compounds. The inset, in (b), depicts the calculated β values for all compounds and pNA.

With the quadratic coefficient obtained by fitting $I(2\omega)$ versus $I^2(\omega)$ following Eq. (3), a linear dependence of this coefficient as a function of the molecular concentration is observed. Figures 6(a) and (b) display $I(2\omega)/I^2(\omega)$ (open symbols) as a function of the concentration for the derivatives **I-III** and pNA. Solid lines represent the best linear fit, in which the angular coefficients were used to determine β

values by using Eq. (4). The value of β_{pNA} is known from the literature. One can see that the linear fits have different slope comparing each sample with pNA. pNA shows a greater slope comparing to **I-III**; thus it is expected that β 's for all three samples are smaller than the standard sample. From the inset of Fig. 6(b), it is possible to see, as column graphic, the experimentally calculated first hyperpolarizability values of all samples studied. β values of the three compounds are very similar, in which compound **III** has the lower value. In general, the first hyperpolarizabilities of these compounds are in agreement with other chalcone derivatives found in the literature (Vaz *et al.*, 2016; Custodio, D'Oliveira *et al.*, 2019).

The order of magnitude of the first hyperpolarizabilities (β) of all three chalcones derivatives can be predicted by knowing μ_{01} and $\Delta\mu_{01}$ values. The greater these quantities are, the higher the incoherent optical second harmonic generation is. Thus, β can be estimated employing a simplified two-level model approach (Lemes *et al.*, 2018). It consists of, firstly, determining static first-order hyperpolarizability β_0 by:

$$\beta_0(0; 0, 0,) = \frac{3(\mu_{01}^2 \cdot \Delta\mu_{01})}{2(\hbar\omega_{01})^2} \quad (7),$$

in which, $\hbar\omega_{01}$ is the energy of the first electronic transition obtained from the linear absorption spectrum (3.5 eV for **I**, 3.8 eV for **II** and 3.9 eV for **III**). The optical frequency dispersion (ω) is taken into account in order to evaluate the dynamical β by employing the undamped two-level model (Oudar, 1977; Campo *et al.*, 2008; Orr & Ward, 1971), which is enhanced by the proximity of the electronic resonance (resonance enhancement). The dynamical β is estimated by:

$$\beta_{2LM}(-2\omega; \omega, \omega) = \frac{\omega_{01}^4}{(\omega_{01}^2 - 4\omega^2)(\omega_{01}^2 - \omega^2)} \beta_0 \quad (8).$$

The estimated values for dynamical β_{2LM} were calculated at 1064 nm (~ 1.17 eV) and are of the same order of magnitude for **I-III**. For compound **I**, which has the highest $\Delta\mu_{01}$, $\beta_{2LM}(2\omega)$ has a value of about 30×10^{-30} cm⁵/esu. Compounds **II** and **III** have values of $\beta_{2LM}(2\omega)$ smaller than compound **I**, of about 21×10^{-30} cm⁵/esu and 19×10^{-30} cm⁵/esu respectively, because the difference between the excited and ground state permanent dipole moments gives a smaller number than for **I**. In Figure 7, one can see the estimated values obtained by using the simplified undamped model compared with the experimental for all three studied samples, the error bars are considered to be of about 15%, due to laser intensity fluctuation.

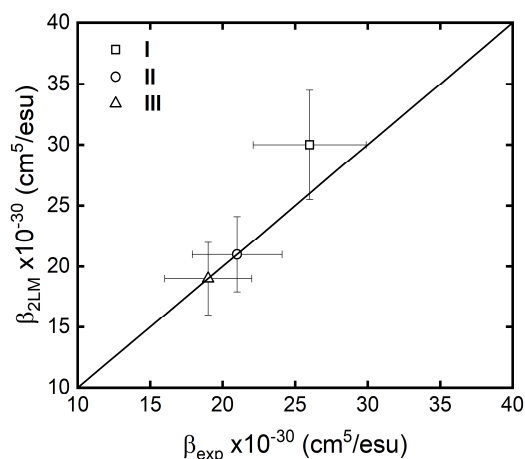


Figure 7 Estimated dynamic first-order hyperpolarizability by the simplified undamped model compared to the experimental of all five studied compounds.

The experimental values obtained for **I-III** are of the same order of magnitude to the estimated values, obtained from an undamped two-level model (Eq. 8). Considering experimental error, we can state that β values of compound **II** and **III** are identical when compared to their respective estimated values, showing that the parameters obtained with one- and two-photon absorption are in agreement with the HRS signal. However, the measured β for compound **I** is 30% lower than that from the estimated β_{2LM} . One explanation for this difference is associated to the energy of the lower absorption band. For this molecule, the energy of the transition is reduced because of the redshift in the absorption band. The energy value is part of Eqs. 7 and 8 as the denominator. Also, in Eq. 8 the dispersion term, which enhances the effect due to the proximity of the transition, is also influenced by this energy. With a redshift, the effect at 1064 nm is overestimated by the undamped two-level model. However, if the error bar of the measurement is considered (about 15%), all values, for measured and estimated ones, are considered statistical identical.

3.3. Thermal characterization

The thermal behaviour of the crystalline compounds **I**, **II** and **III** was studied by a combination of DSC, TGA and HSM techniques, and the results are presented in Figure 8. Both **I**, **II** and **III** are stable between 25 and 130 °C and their DSC curves exhibit endothermic melting peaks between 130 and 160 °C. DSC curves of **I** and **III** are characterized by a single endothermic melting peak at 137.66 °C ($T_{\text{onset}} = 131.47$ °C) and 157.63 °C ($T_{\text{onset}} = 149.03$ °C), respectively, which were attributed to the fusion of the samples. Meanwhile, in DSC curves of compounds **I** and **III**, over 320 °C, exothermic events can be observed; for **III** there is a clear exothermic peak at 328.25 °C ($T_{\text{onset}} = 316.13$ °C). In both cases these peaks are attributed to the decomposition of the samples. These values agree with the gradual mass loss

that occurs in the TGA curves which begins around 260 °C ($T_{\text{onset}} = 264.85$ °C for **I** and $T_{\text{onset}} = 283.22$ °C for **III**).

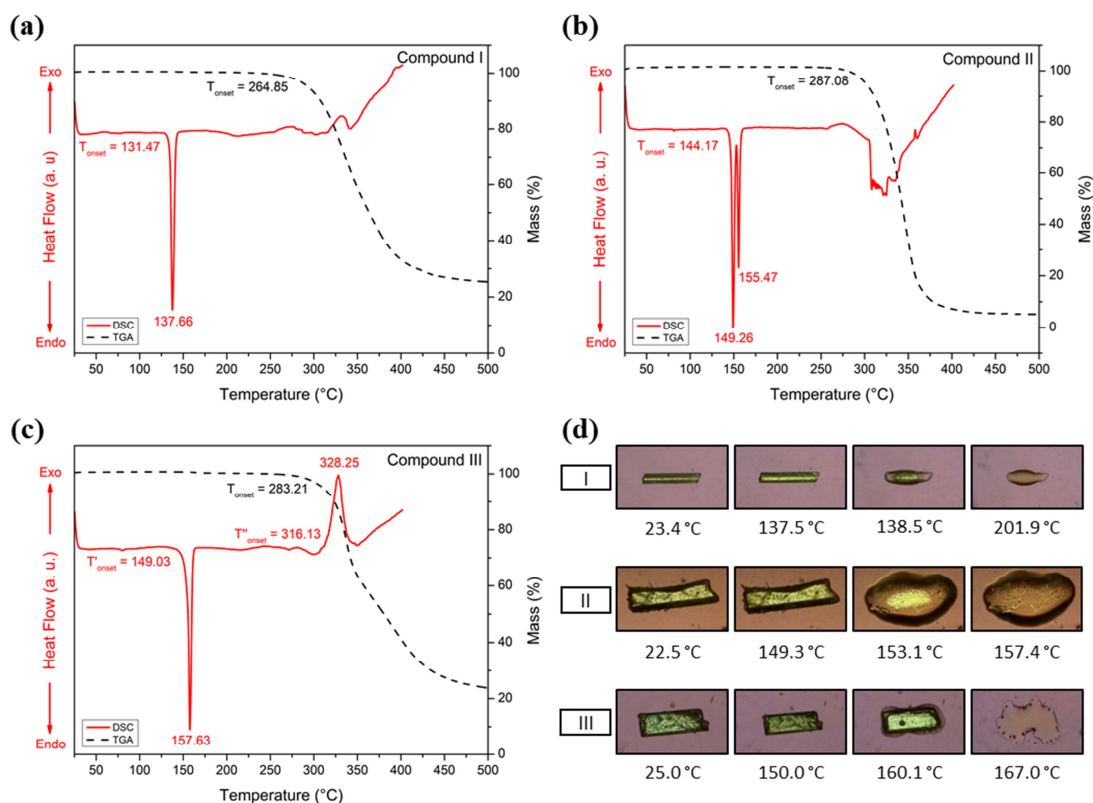


Figure 8 Thermal analysis. DSC, TGA curves and Hot-stage microscopy images of compounds **I**, **II** and **III**, respectively.

The melting point of **II** is assigned to dual endothermic peaks at 149.26 °C and 155.47 °C ($T_{\text{onset}} = 144.17$ °C) in the DSC curve. Unlike **I** and **III**, compound **II** presents a new endothermic-like pattern over 280 °C, related to decomposition of the sample. This event is accompanied by the thermal decomposition of the sample because of a gradual mass loss in the TGA curve up to 280 °C ($T_{\text{onset}} = 287.06$ °C) can be observed. In comparison, compound **I** has the lowest thermal stability. HSM was also performed in order to visualize the thermal events described above. Although HSM and DSC/TGA experiments were performed under different atmospheres, the results are in good agreement to each other. From HSM images (Fig. 8), it is possible to see that **I**, **II** and **III** crystals undergo fusion at around 138 °C, 153 °C and 160 °C, respectively. The images also show the beginning and complete melting of the crystals which are in agreement to DSC curves. It is worth to

mention that, according to DSC curves, there is evidence of other peaks that could be associated with different phase transitions such as evaporation, but such behaviour was not observed in HSM.

4. Conclusion

The three sulphonamide chalcone derivatives discussed here have a common backbone with different substituents at *para* position of ring B. Compound **I** crystallizes in monoclinic system whereas the crystal packing of **II** and **III** are triclinic. **I**, **II**, and **IIIa** could be consider planar molecules while **IIIb** is not, because there is an angle of 16.37° between the planes of ring A and B. The effect of halogen substituents changing, chlorine (**II**) by bromine (**III**) can be noticed in **IIIa** due to the greatest angle formed by the A and B rings. Finally, C–H···O interactions dominates the packing of these compounds. All compounds form dimers and arrangements where two accepting sites share one donor atom.

Nonlinear optical properties showed that the atoms or group added to the main structure of chalcone studied do not modify significantly values of β nor σ_{2PA} . The spectrum obtained shown that the first excited state is permitted both by 1PA and 2PA, indicating that there is an asymmetric charge distribution along the π -conjugated molecule structure. σ_{2PA} spectra of compounds **II** and **III** show an excited state that is permitted by 2PA. NLO properties of compounds I-III agree with other chalcones previously studied, which indicates that adding the benzenosulfonyl group does not influence these properties. Comparing HRS experimental results and theoretical model, estimated and experimental β values obtained are in good agreement. Considering the similar experimental values for different substituents, these results motivate further investigation on substituent-based optical properties for other sulphonamide-chalcone hybrids.

5. Acknowledgements

The authors gratefully acknowledge the financial support of the Conselho Nacional de desenvolvimento Científico e Tecnológico (CNPq), Fundação de Amparo à Pesquisa do Estado de Goiás (FAPEG), Fundação de Amparo à Pesquisa do Estado de São Paulo (FAPESP – Brazil; Grants 2016/20886-1 and 2018/11283-7), INCT-FOTÔNICA Army Research Laboratory W911NF-17-1-0123 and Air Force Office of Scientific Research (FA9550-12-1-00258). We also thank to Coordenação de Aperfeiçoamento de Pessoal de Nível Superior - Brasil (CAPES) - Finance Code 001 for the financial support.

References

- Abegão, L. M. G., Fonseca, R. D., Ramos, T. N., Mahuteau-Betzer, F., Piguel, S., Joatan R., J., Mendonça, C. R., Canuto, S., Silva, D. L. & De Boni, L. (2018). *J. Phys. Chem. C*. **122**, 10526–10534.
- Abegão, L. M. G., Fonseca, R. D., Santos, F. A., Souza, G. B., Barreiros, A. L. B. S., Barreiros, M. L., Alencar, M. A. R. C., Mendonça, C. R., Silva, D. L., De Boni, L. & Rodrigues, J. J. (2016). *Chem. Phys. Lett.* **648**, 91–96.
- Allen, F. H. (2002). *Acta Crystallogr. Sect. B Struct. Sci.* **58**, 380–388.
- Bruker (2012). *Apex 2*. Bruker AXS Inc., Madison, Wisconsin, USA. [Older versions (pre-1997) should refer to Siemens Analytical X-ray Instruments Inc. instead of Bruker AXS.
- Campo, J., Wenseleers, W., Goovaerts, E., Szablewski, M. & Cross, G. H. (2008). *J. Phys. Chem. C*. **112**, 287–296.
- Castro, M. R. C. de, Aragão, A. Q., Napolitano, H. B., Noda-Perez, C. & Martins, F. T. (2013). *Acta Crystallogr. Sect. C Cryst. Struct. Commun.* **69**, 267–272.
- De Castro, M. R. C., Aragão, Â. Q., Da Silva, C. C., Perez, C. N., Queiroz, D. P. K., Júnior, L. H. K. Q., Barreto, S., De Moraes, M. O. & Martins, F. T. (2016). *J. Braz. Chem. Soc.* **27**, 884–898.
- De Castro, M. R. C., Naves, R. F., Bernardes, A., da Silva, C. C., Perez, C. N., Moura, A. F., de Moraes, M. O. & Martins, F. T. (2020). *Arab. J. Chem.* **13**, 1345-1354
- Chandra Shekhara Shetty, T., Raghavendra, S., Chidan Kumar, C. S., Naveen, S., Maidur, S. R., Patil, P. S., Chandraju, S., Ananthnag, G. S. & Dharmaparakash, S. M. (2018). *Opt. Mater. (Amst)*. **86**, 138–147.
- Clays, K. & Persoons, A. (1992). *Rev. Sci. Instrum.* **63**, 3285–3289.
- Custodio, J. M. F., D'Oliveira, G. D. C., Gotardo, F., Cocca, L. H. Z., De Boni, L., Perez, C. N., Maia, L. J. Q., Valverde, C., Osório, F. A. P. & Napolitano, H. B. (2019). *J. Phys. Chem. C*. **123**, 5931–5941.
- Custodio, J. M. F., Vaz, W. F., de Castro, M. R. C., Bernardes, A., Naves, R. F., Moura, A. F., de Moraes, M. O., da Silva, C. C., Martins, F. T., Perez, C. N. & Napolitano, H. B. (2019). *J. Mol. Struct.* **1175**, 389–397.
- Custodio, J., Michelini, L., Castro, M., Fonseca Vaz, W., Neves, B. J., Cravo, P., Barreto, F., de Moraes, M. O., Perez, C. & Napolitano, H. (2018). *New J. Chem.* **42**, 3426-3434.
- D'silva, E. D., Podagatlapalli, G. K., Venugopal Rao, S. & Dharmaparakash, S. M. (2012). *Mater. Res.*

- Bull.* **47**, 3552–3557.
- Dolomanov, O. V., Bourhis, L. J., Gildea, R. J., Howard, J. A. K. & Puschmann, H. (2009). *J. Appl. Crystallogr.* **42**, 339–341.
- Franzen, P. L., Misoguti, L. & Zilio, S. C. (2008). *Appl. Opt.* **47**, 1443.
- Göppert-Mayer, M. (2009). *Ann. Der Physik.* **18**, 466–479.
- Govindasamy, P. & Gunasekaran, S. (2015). *J. Mol. Struct.* **1081**, 96–109.
- Groom, C. R. & Allen, F. H. (2014). *Angew. Chemie - Int. Ed.* **53**, 662–671.
- Kamada, K., Ohta, K., Iwase, Y. & Kondo, K. (2003). *Chem. Phys. Lett.* **372**, 386–393.
- Kamal, A., Mallareddy, A., Suresh, P., Shaik, T. B., Lakshma Nayak, V., Kishor, C., Shetti, R. V. C. R. N. C., Sankara Rao, N., Tamboli, J. R., Ramakrishna, S. & Addlagatta, A. (2012). *Bioorganic Med. Chem.* **20**, 3480–3492.
- Kumar, P. C. R., Ravindrachary, V., Janardhana, K., Manjunath, H. R., Karegouda, P., Crasta, V. & Sridhar, M. A. (2011). *J. Mol. Struct.* **1005**, 1–7.
- Lemes, S. R., Júnior, L. A., da Silva Manoel, D., de Sousa, M. A. M., Fonseca, R. D., Lima, R. S., Noda-Perez, C., de Melo Reis, P. R., Cardoso, C. G., de Paula Silveira-Lacerda, E., Souza, M. A. R., Mendonça, C. R., Gonçalves, P. J., de Boni, L., da Fonseca, T. L. & da Silva Junior, N. J. (2018). *Spectrochim. Acta Part A Mol. Biomol. Spectrosc.* **204**, 685–695.
- Lin, Y., Zhou, Y., Flavin, M. T., Zhou, L., Nie, W. & Chen, F. (2002). *Bioorganic Med. Chem.* **10**, 2795–2802.
- Macrae, C. F., Bruno, I. J., Chisholm, J. a., Edgington, P. R., McCabe, P., Pidcock, E., Rodriguez-Monge, L., Taylor, R., van de Streek, J. & Wood, P. a. (2008). *J. Appl. Crystallogr.* **41**, 466–470.
- Mahapatra, D. K. & Bharti, S. K. (2016). *Life Sci.* **148**, 154–172.
- Makhlouf, M. M., Radwan, A. S. & Ghazal, B. (2018). *Appl. Surf. Sci.* **452**, 337–351.
- Menezes, A. P., Jayarama, A. & Ng, S. W. (2015). *J. Mol. Struct.* **1088**, 85–94.
- Nardelli, M. (1995). *J. Appl. Crystallogr.* **28**, 659–659.
- Neves, U. M., De Boni, L., Ye, Z., Bu, X. R. & Mendonça, C. R. (2007). *Chem. Phys. Lett.* **441**, 221–225.
- Onsager, L. (1936). *J. Am. Chem. Soc.* **58**, 1486–1493.
- Orr, B. J. & Ward, J. F. (1971). *Mol. Phys.* **20**, 513–526.

- Oudar, J. L. (1977). *J. Chem. Phys.* **67**, 446–457.
- Ražna, J., Hodge, P., West, D. & Kucharski, S. (1999). *J. Mater. Chem.* **9**, 1693–1698.
- Rigaku, O. D. (2015). *CrysAlis PRO*. Rigaku Oxford Diffraction, Yarnton, England.
- Sarajini, K., Krishnan, H., Kanakam, C. C. & Muthu, S. (2013). *Spectrochim. Acta Part A Mol. Biomol. Spectrosc.* **108**, 159–170.
- Seo, W. D., Ryu, Y. B., Curtis-Long, M. J., Lee, C. W., Ryu, H. W., Jang, K. C. & Park, K. H. (2010). *Eur. J. Med. Chem.* **45**, 2010–2017.
- Sheik-Bahae, M., Said, A. A., Wei, T.-H., Hagan, D. J. & Stryland, E. W. Van (1990). *IEEE J. Quantum Electron.* **26**, 760–769.
- Sheldrick, G. (2008). *Acta Crystallogr. Sect. A.* **64**, 112–122.
- Sheldrick, G. M. (2015). *Acta Crystallogr. Sect. A Found. Adv.* **71**, 3–8.
- Singh, P., Anand, A. & Kumar, V. (2014). *Eur. J. Med. Chem.* **85**, 758–777.
- Spek, A. L. (2009). *Acta Crystallogr. Sect. D.* **65**, 148–155.
- Tajuddeen, N., Isah, M. B., Suleiman, M. A., van Heerden, F. R. & Ibrahim, M. A. (2018). *Int. J. Antimicrob. Agents.* **51**, 311–318.
- Vaz, W. F., Custodio, J. M. F., Silveira, R. G., Castro, A. N., Campos, E. M., Anjos, M. M., Oliveira, G. R., Valverde, C. & Napolitano, H. B. (2016). *RSC Adv.* **6**, 79215–79227.
- Zhai, L., Chen, M., Blom, J., Theander, T. G. & Kharazmi, A. (1999). *J. Antimicrob. Chemother.* **43**, 793–803.

Highlights

- A set of three new sulfonamide chalcones was synthesized;
- Their chemical structures were analyzed from SCXRD and were found to be different from each other;
- NLO properties of the synthesized compounds were not affected by the structural differences;

Journal Pre-proof

Declaration of interests

The authors declare that they have no known competing financial interests or personal relationships that could have appeared to influence the work reported in this paper.

The authors declare the following financial interests/personal relationships which may be considered as potential competing interests: